ACS OMEGA

Open Access

http://pubs.acs.org/journal/acsodf

Article

In Vitro Ferroptotic and Antitumor Effect of Free or Liposome-Encapsulated Artesunate in Papillary Thyroid Cancer Cells

Li Sun, Guangzhe Zheng, Meng Zhou, Yingyu Zhang, Yashuang Yang, Shuping Zhang,* and Ling Gao*

Cite This: *ACS Omega* 2024, 9, 7463−7470

Read Online

ACCESS | Metrics & More | Article Recommendations | Supporting Information

ABSTRACT: Papillary thyroid cancer (PTC) is generally treated as an indolent and curable cancer. However, the unavailability of surgery and ineffective radiotherapy persists in PTCs, resulting in poor outcomes and low survival rates. Thus, new chemotherapeutic strategies for PTCs are urgently needed. Resistance to ferroptosis remarkably contributes to cancer occurrence and progression. Artesunate (ART) has been repurposed as an anticancer drug, as it induces cell death in numerous cancers. However, whether ART induces ferroptosis in PTC cells and, consequently, facilitates PTC therapy remains elusive. Furthermore, overcoming the pharmacological limitations of ART is a key requirement to support its clinical application. Herein, we reanalyzed the Cancer Genome Atlas (TCGA) and Genotype-Tissue Expression database (GTEx) to characterize the occurrence of resistance to ferroptosis in thyroid cancer. In vitro results showed that ART induced ferroptosis in PTC cells by increasing the cellular iron content. The encapsulation of ART by liposomes did not alter the efficiency in inducing ferroptosis and inhibiting the invasion and migration of PTC cells compared with direct ART application. Thus, PTC resistance to ferroptosis can be overcome by ART and liposome-encapsulated ART.

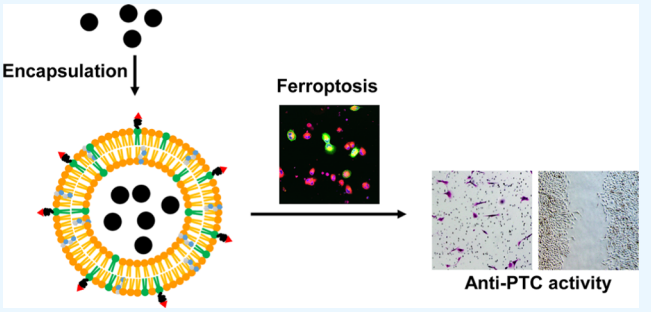

INTRODUCTION

Thyroid cancer is among the most common cancers, with increasing cases worldwide. It primarily occurs as papillary thyroid cancer (PTC) and follicular thyroid cancer (FTC).[1,2] Based on genetic alterations, including BRAF and RAS mutations and RET/PTC chromosomal rearrangements, PTCs can be divided into BRAF-like or RAS-like subtypes with distinct biological features and aggressiveness.[3] Although the 10-year survival rate for PTCs is usually >90% when diagnosed early, recurrence and metastasis render surgery unavailable and radiotherapy ineffective, leading to a very low survival rate.[1,4] Developing new chemotherapeutic strategies is important for the effective treatment of PTCs.

Ferroptosis is a newly identified and iron-dependent form of programmed cell death (PCD).[5] As characterized by lipid peroxidation, ferroptosis is distinct from other PCDs, such as apoptosis, necrosis, and autophagy, and has been implicated in various pathological conditions and diseases.[6] Resistance to ferroptosis has also been associated with cancer resistance to chemotherapy, radiotherapy, and immunotherapy.[7] Ferroptosis induction may provide a new opportunity to overcome therapy resistance in cancers.

Artesunate (ART) is a derivative of artemisinin and a first-line drug for malaria therapy.[8] It has been repurposed as an anticancer drug because it induces multiple forms of PCD, including apoptosis, autophagy, and ferroptosis.[9] ART induces apoptosis and inhibits the proliferation and migration of thyroid cancer cells by inhibiting the PI3K/AKT/FKHR signaling pathway.[10] However, whether ART induces ferroptosis in PTC cells and improves PTC therapy remains elusive. Similar to other artemisinin derivatives, ART is pharmacologically limited owing to its poor bioavailability and water solubility, short half-life, and side effects after long-term usage.[11] Thus, exploiting new delivery strategies is necessary to support the clinical applications of ART in cancer therapy.

This study identified ferroptosis resistance in thyroid cancers and demonstrated ART-induced ferroptosis in PTC cells. Liposomes, a common nanoparticle used for drug delivery and approved by the Food and Drug Administration (FDA), were used to deliver ART. Liposome-encapsulated ART (LIP@ART) preserved the efficiency of ART in inducing ferroptosis and inhibiting the invasion and migration of PTC cells.

MATERIALS AND METHODS

Analysis of Ferroptosis Marker Genes in TCGA and GTEx Databases. A gene set of 39 ferroptosis markers was

Received: July 20, 2023
Revised: January 18, 2024
Accepted: January 24, 2024
Published: February 7, 2024

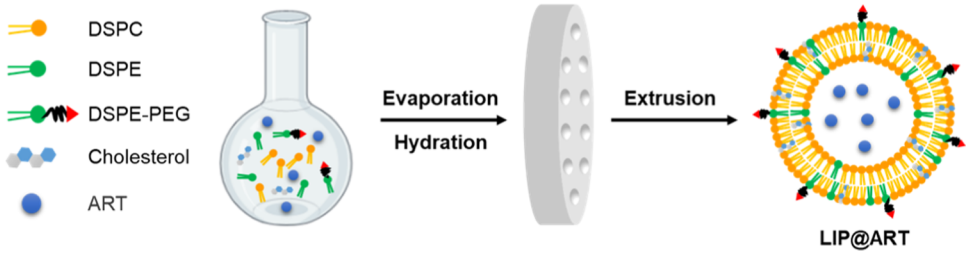

Figure 1. Schematic diagram for the synthesis of LIP@ART.

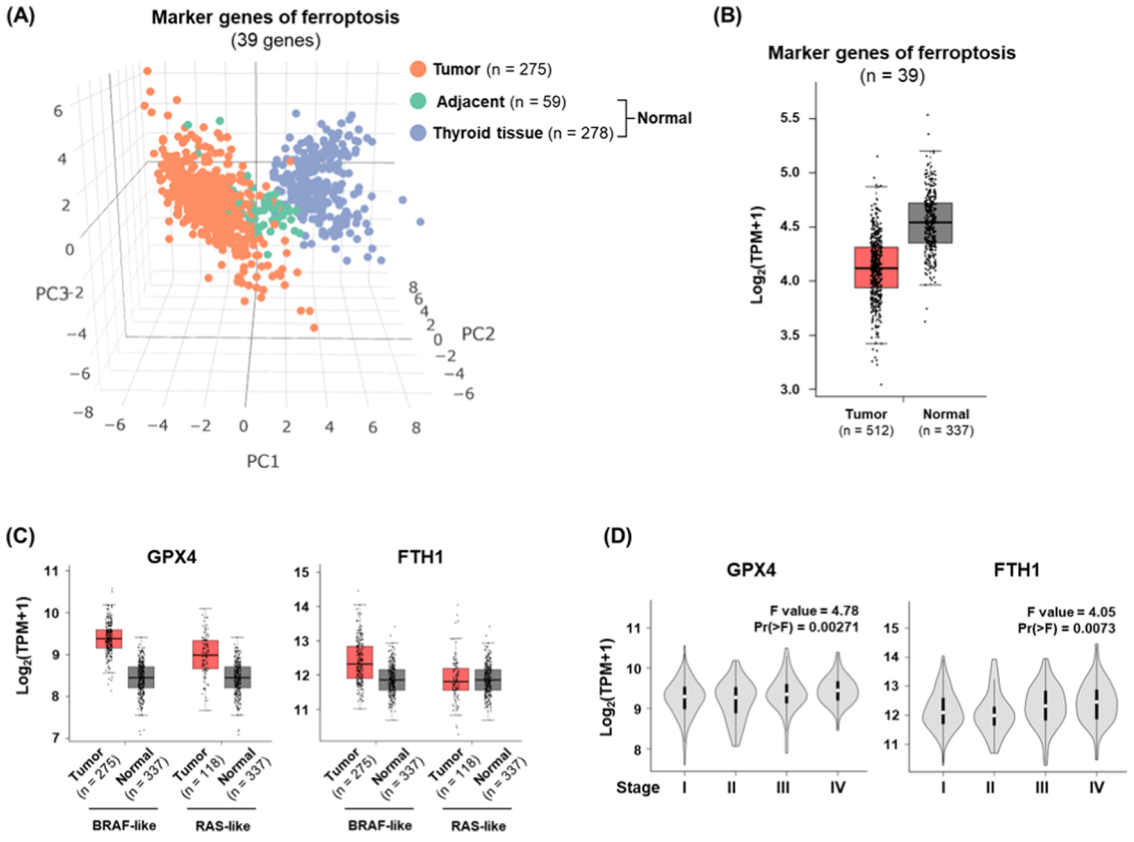

Figure 2. Resistance of thyroid cancer to ferroptosis. (A, B) PCA dimensionality reduction (A) and expression (B) of 39 ferroptosis marker genes in thyroid cancer and normal tissue samples from the thyroid cancer data set (THCA) of Cancer Genome Atlas (TCGA) and Genotype-Tissue Expression database (GTEx). Marker genes of ferroptosis were curated from FerrDb.[12] (C) Expression levels of GPX4 and FTH1 in thyroid cancer and normal tissue samples from TCGA and GTEx. (D) Expression levels of GPX4 and FTH1 in thyroid cancer samples of different pathological stages from TCGA and GTEx.

curated from FerrDb (Table S1).[12] GEPIA2 (http://gepia2.cancer-pku.cn/) was used to perform the PCA dimensionality reduction and scoring of this ferroptosis gene set in thyroid cancer and normal tissue samples from the thyroid cancer (THCA) data set in the Cancer Genome Atlas (TCGA) and Genotype-Tissue Expression database (GTEx). Expression of gene sets or genes is represented as $Log_2(TPM + 1)$.

Synthesis of LIP@ART. A thin-film rehydration method was used to synthesize LIP@ART (Figure 1). DSPC, cholesterol, DSPE, DSP-PEG, and ART were dissolved in 1 mL of chloroform (solution 1). DSPE was dissolved in 1 mL of a mixture of chloroform−methanol−deionized water (6:3:1, v/v; solution 2). Then, solutions 1 and 2 were added to a round-bottom flask and mixed well at 40 °C. After evaporation with spinning for 30 min, a homogeneous thin film was formed, followed by rehydration with PBS for 1 h. After sonication for 30 min (a total of 12 cycles of 15 s), the liposome solution was extruded 6 times using a liposome extruder and an extrusion membrane (400 or 200 nm pore size). The extruded solution was centrifuged (20,000*g* for 10 min), and the LIP@ART precipitate was collected. Lyophilized LIP@ART powder was obtained by freeze-drying. Meanwhile, the supernatant was used for the drug loading content (DLC) measurement.

Characterization of LIP@ART. Transmission electron microscopy (TEM) was used to visualize LIP and LIP@ART (HT7800, Hitachi, Japan). Hydrodynamic diameter distribution and ζ-potentials were measured by using a Zetasizer (Malvern Nanoseries, U.K.). Ultraviolet−visible (UV−vis) adsorption spectra were monitored with a TU-1901 spectrophotometer (Hitachi, Japan).

The supernatant was diluted in methanol for the DLC assay and measured by high-performance liquid chromatography. The amount of LIP-encapsulated ART was calculated against a standard curve of ART:DLC (%) = (weight of ART

https://doi.org/10.1021/acsomega.3c05226
ACS Omega 2024, 9, 7463−7470

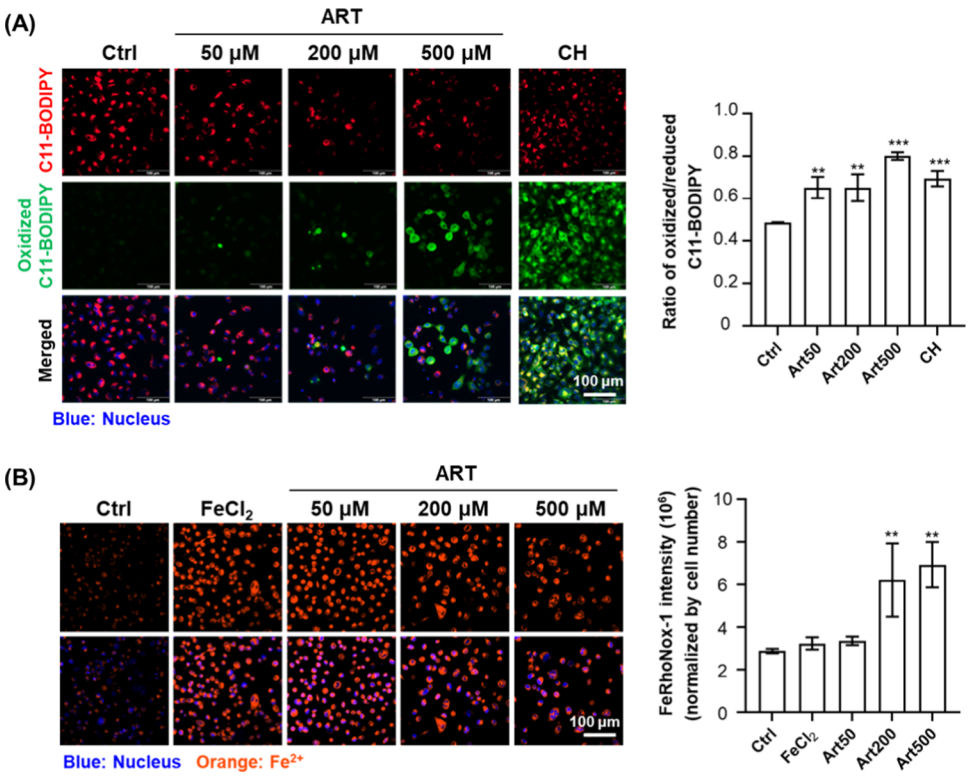

Figure 3. Artesunate-induced ferroptosis and increased ferrous iron in PTC cells. (A) Representative images and quantitative data of ferroptosis as indicated by lipid peroxidation in B-CPAP cells. After incubation with ART (50−500 μM) for 24 h, the cells were stained with an Image-iT lipid peroxidation staining kit (C11-BODIPY) for confocal analysis, and cell nuclei were stained with NucBlue Live Ready Probes (Hoechst 33342). Cells treated with 100 μM cumene CH for 2 h were used as a positive control. Scale bar: 100 μm. (B) Representative images and quantitative data of cellular ferrous iron (Fe^{2+}). B-CPAP cells treated with ART (50−500 μM) for 24 h were stained with a live-cell Fe^{2+} probe (FeRhoNox-1) to visualize cellular Fe^{2+} (in red). Cells treated with 100 μM $FeCl_2$ were used as positive control. Hoechst 33342 was used to label cell nuclei (in blue). Scale bar: 100 μm. Data are presented as mean ± SD. $^{**}P < 0.01$, $^{***}P < 0.001$.

encapsulated inside the LIP@ART/total weight of LIP@ART) × 100%.

Cell Culture. The PTC cell line B-CPAP was purchased from the Cell Bank/Stem Cell Bank of the Chinese Academy of Sciences (Shanghai, China). Cells were cultured at 37 °C with 5% CO_2 in DMEM with 4.5 g/L glucose (Gibco, USA), supplemented with 10% fetal bovine serum (Sijiqing, China) and 100 U/mL penicillin−streptomycin (Gibco, USA).

Lipid Peroxidation and Ferrous Iron Content. To assess lipid peroxidation, B-CPAP cells (4×10^4/well) were plated in 8-well chambered cover glasses (ThermoFisher Scientific, USA) and incubated overnight at 37 °C. The cells were treated with 50−200 μM ART or 200 μM LIP@ART for 24 h or 100 μM cumene hydroperoxide (CH) for 2 h as a positive control. After washing twice with PBS, the cells were stained with C11-BODIPY from an Image-iT lipid peroxidation kit and Hoechst 33342 (Invitrogen, USA) for 0.5 h at 37 °C. The stained cells were then washed with PBS and kept in live-cell imaging solution (LCIS) (Invitrogen, USA). The fluorescence of oxidized C11-BODIPY and reduced C11-BODIPY was detected through the 488 and 561 nm channels, respectively, using confocal microscopy (FV12-IXCOV, Olympus, Japan). Subsequently, we utilized cellSens software (Olympus, Japan) to measure the fluorescence values of the 488 and 561 nm channels in at least three independent fields for each group. The ratio of these values represents the "Ratio of oxidized/reduced C11-BODIPY", reflecting the level of cellular lipid peroxidation.

To detect cellular 4-HNE (4-Hydroxynonenal), B-CPAP cells (1×10^5/well) were plated into 12-well plates and cultured overnight at 37 °C. The cells were treated with 200 μM ART or 200 μM LIP@ART and co-treated with or without 50 μM DFO. After treatment, the cells were collected and lyzed to detect cellular 4-HNE by a 4-HNE ELISA kit (Shanghai Jianglai Industrial Limited By Share Ltd., China).

To measure the cellular content of ferrous iron, cells were treated with 50−200 μM ART, 200 μM LIP@ART, or 100 μM $FeCl_2$ for 24 h. After washing with PBS, the cells were stained with FeRhoNox-1 (Goryo Chemical, Japan) in serum-free PBS and Hoechst 33342 for 1 h. After washing with PBS, the stained cells were kept in LCIS and imaged by confocal microscopy at emission wavelengths of 405 (nucleus) and 488 nm (Fe^{2+}) (FV12-IXCOV, Olympus, Japan).

Western Blotting. The protein of B-CPAP cells was extracted by RIPA lysis buffer (Solarbio, China) with 1% PMSF (Solarbio, China). Equal amounts of denatured proteins were subjected to SDS-PAGE and then transferred to NC membranes (ThermoFisher Scientific, USA). The NC membranes were blocked with 5% BSA (Bioshark, China) in TBST for 1 h and then incubated with 1:1000 diluted primary antibodies/anti-GPX4 (glutathione peroxidase 4) rabbit IgG (Cat. ab125066, Abcam, U.K.), anti-SLC7A11 (solute Carrier Family 7 Member 11) rabbit IgG (Cat. Ab216876, Abcam, U.K.), anti-ACSL4 (acyl-CoA synthetase long-chain family member 4) rabbit IgG (Cat. 155282, Abcam, U.K.), and anti-GAPDH rabbit IgG (Cat. 10494−1-AP, Proteintech, China).

https://doi.org/10.1021/acsomega.3c05226
ACS Omega 2024, 9, 7463−7470

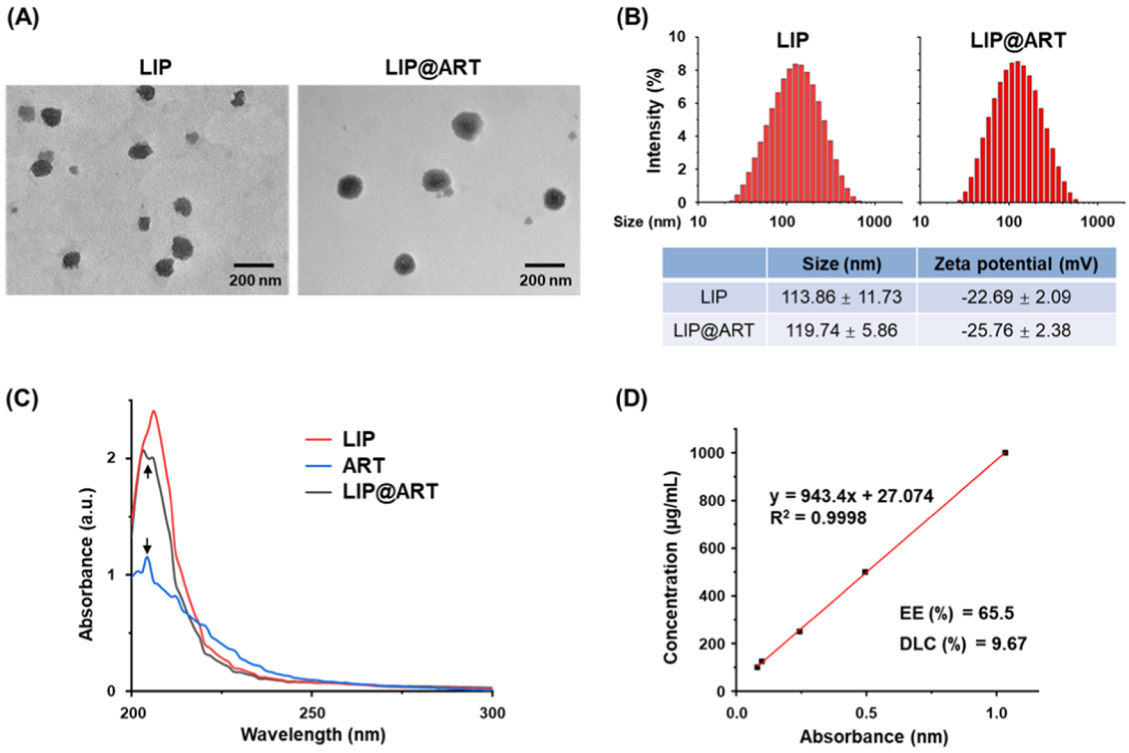

	Size (nm)	Zeta potential (mV)
LIP	113.86 ± 11.73	-22.69 ± 2.09
LIP@ART	119.74 ± 5.86	-25.76 ± 2.38

Figure 4. Synthesis and characterization of LIP@ART. (A) Representative TEM images of liposome (LIP) and liposome-encapsulated artesunate (LIP@ART). (B) Hydrodynamic diameter distribution and ζ-potentials of LIP and LIP@ART. (C) Ultraviolet−visible (UV−vis) absorbance spectra of LIP, ART, and LIP@ART. Arrows indicate an absorbance peak of ART around 204 nm. (D) Encapsulation efficiency (EE) and drug loading content (DLC) of ART in LIP@ART. The amount of ART encapsulated by LIP was calculated against a standard curve using the following formula: DLC (%) = (weight of ART encapsulated inside the LIP@ART/total weight of LIP@ART) × 100%.

Next, the NC membranes were incubated with goat antirabbit IgG (Cat. SA00001-2, Proteintech, China) for 1 h and imaged on the ChemiDoc XRS+ gel imaging system (Bio-Rad, USA).

Cell Viability Assay. To detect the cell viability, the B-CPAP cells were seeded into a 96-well plate and cultured overnight. The cells were treated with 200 μM ART or ART@LIP and co-treated with 50 μM DFO for 24 h. After treatment, the culture medium was removed, and the Alamar Blue work solution (40 μM resazurin sodium in medium) was added into wells. After incubation for 2 h, the fluorescence intensity of resorufin of each well was detected on a Varioskan LUX microplate reader (ThermoFisher Scientific, USA).

B-CPAP cells (4×10^4) were seeded into a 96-well flat clear bottom black microplate (Corning, USA) and cultured overnight. Upon treatment with 200 μM ART or ART@LIP for 24 h, the culture medium was removed, and the cells were stained by the Calcein/PI working solution (Calcein AM and PI were diluted with PBS at a ratio of 1:1000; Beyotime, China) followed by incubation at 37 °C in the dark for 30 min. After incubation, the fluorescence intensity of Calcein (Ex/Em = 494:517 nm) and PI (535/617 nm) was measured on a Varioskan LUX microplate reader. The ratios of the fluorescence intensity of Calcein/PI of each well were then analyzed.

Cell Invasion and Migration Assay. Transwell invasion assays were used to investigate the invasion of B-CPAP cells using a 24-well transwell chamber (Corning, USA). Briefly, B-CPAP cells (4×10^4) were seeded into the upper chamber precoated with Matrigel (BD, USA) and treated with 200 μM ART or LIP@ART. The lower chamber was filled with 600 μL culture medium. After 24 h, B-CPAP cells on the upper side of the membrane were removed and cells from seven randomly selected fields on the underside were imaged and counted under an Axio Vert.A1 fluorescence inverted microscope (Zeiss, Germany).

A wound healing assay was performed to investigate the migration of the B-CPAP cells. Briefly, a monolayer of B-CPAP cells was uniformly seeded in a six-well plate and then wounded by scratching the surface with a 200-μL pipet tip. After washing 3 times with PBS, the cells were treated with 200 μM ART or LIP@ART for 24 h. The initial wound and the movement of cells into the scratched area were imaged at 0 and 24 h under an Axio Vert.A1 fluorescence inverted microscope (Zeiss, Germany). The wound width was measured in five randomly selected fields, and the migration rate of the cells was calculated as the wound width at 0 h minus the wound width at 24 h following normalization by the wound width at 0 h.

Statistical Analysis. One-way analysis of variance (ANOVA) and *t*-test were used to analyze differences between >3 groups and between 2 groups, respectively. All data are presented as mean ± standard error (SD). $P < 0.05$ was considered statistically significant.

RESULTS AND DISCUSSION

Ferroptosis Resistance in Thyroid Cancer. To determine whether ferroptosis resistance occurs in thyroid cancer, we curated a custom gene list containing 39 markers of ferroptosis (Table S1) from FerrDb.[12] Expression of these marker genes was evaluated in the THCA of TCGA and GTEx. Thyroid cancer tissues, adjacent tissues, and thyroid tissues can be distinguished by their expression of ferroptosis

https://doi.org/10.1021/acsomega.3c05226
ACS Omega 2024, 9, 7463−7470

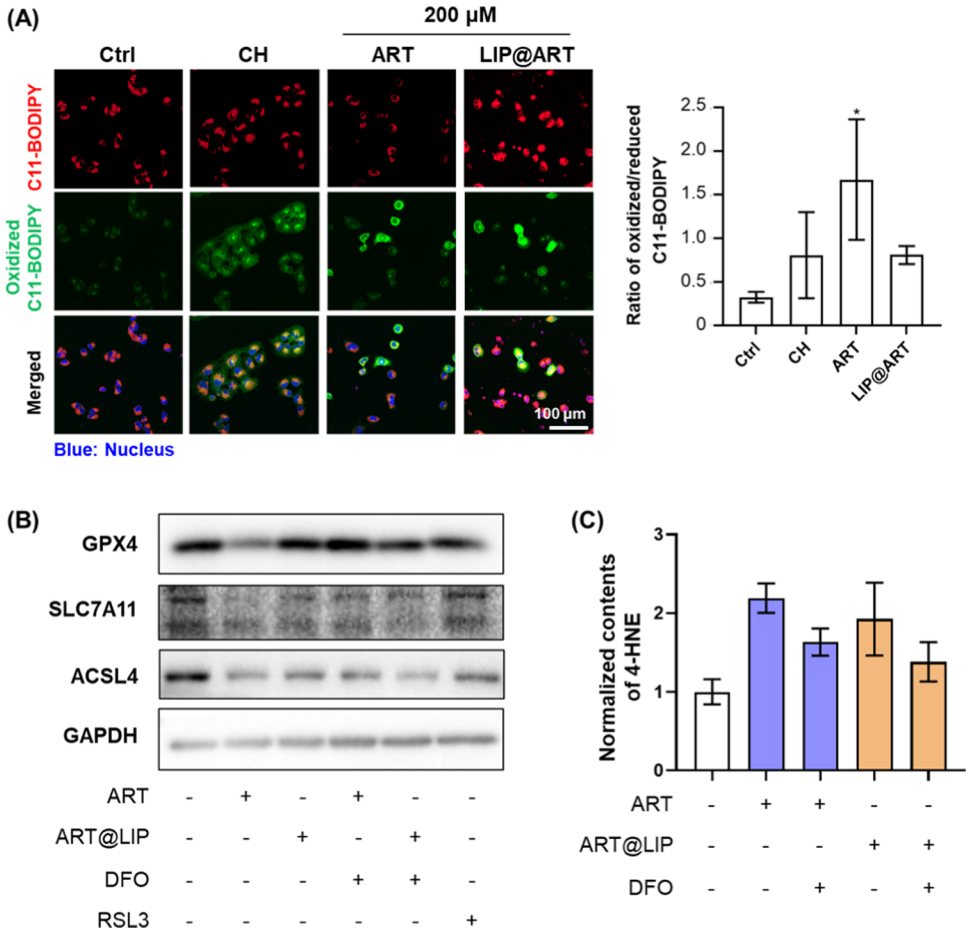

Figure 5. Preserved ferroptotic effect of LIP@ART in PTC cells. (A) Representative images and quantitative data of ferroptosis occurrence indicated by lipid peroxidation in B-CPAP cells. After 24 h exposure to 200 μM ART or LIP@ART, B-CPAP cells were stained with Image-iT lipid peroxidation staining kit (C11-BODIPY) for confocal analysis, and cell nuclei were stained with Hoechst 33342. CH was used as a positive control. Scale bar: 100 μm. Data are presented as mean ± SD *P < 0.05. (B, C) Representative Western blots of GPX4, SLC7A11, and ACSL4 proteins (B), and 4-HNE contents as detected by an ELISA kit (n = 3) in B-CPAP cells (C). The cells were exposed to 200 μM ART or LIP@ART for 24 h, followed by Western blotting analysis or ELISA assay. GAPDH was used as a loading control.

marker genes (Figure 2A). Furthermore, total expression of the ferroptosis marker genes was significantly downregulated in thyroid cancer tissues versus normal adjacent tissues (Figure 2B).

High GPX4 and FTH1 expression is an important prerequisite for 27HC-driven resistance of breast cancer cells to ferroptosis.[13] GPX4 expression was substantially upregulated in BRAF- and RAS-like thyroid cancer tissues compared to normal tissues (Figure 2C). FTH1 expression was also considerably upregulated in the BRAF-like thyroid cancer samples compared to that in the normal tissues (Figure 2C). Furthermore, the expression of GPX4 and FTH1 was stage-dependently upregulated in thyroid cancer (Figure 2D).

Several recent studies have reported that prognosis and immune infiltration in thyroid cancer can be predicted using a ferroptosis-associated gene signature as an independent prognostic index.[14] Moreover, ferroptosis resistance contributes to tumorigenicity and metastasis in many cancers, including breast,[13] gastric,[15] and colorectal cancers.[16] Our analysis also showed ferroptosis resistance in thyroid cancer. Accordingly, chemotherapy resistance induced by ferroptosis resistance can be mechanically reversed by modulating the GPX4-regulated lipid and iron metabolism pathways using a combination of drugs or chemicals.[7]

Induction of Ferroptosis by Artesunate in PTC Cells. We evaluated the ability of ART to induce ferroptosis in B-CPAP cells, which is a commonly used PTC cell line. Lipid peroxidation is the main trigger and canonical maker of ferroptosis.[5] To detect cellular lipid peroxidation in B-CPAP cells exposed to ART, we measured the levels of oxidized C11-BODIPY, a common marker of lipid peroxidation.[5] We found that lipid peroxidation was induced by ART in a dose-dependent manner, as indicated by the increased ratio of the oxidized form (green) to the reduced form (red) of C11-BODIOY compared with that in the untreated cells (Figure 3A).

Active ferrous iron (Fe^{2+}) initiates the Fenton reaction, producing excess ROS and ferroptosis.[6] Similar to the positive control treated with $FeCl_2$, intracellular Fe^{2+} was remarkably increased in ART-treated B-CPAP cells compared to the untreated cells, as indicated by FeRhoNox-1 staining (a substrate reacting with Fe^{2+}; Figure 3B). Furthermore, treatment with the lowest dose, 50 μM, increased cellular Fe^{2+} to a level comparable to that of the positive control (Figure 3B).

Several drugs and chemicals have been reported to produce ferroptotic effects in thyroid cancer cells. For example, curcumin was recently reported to induce ferroptosis in FTC

https://doi.org/10.1021/acsomega.3c05226
ACS Omega 2024, 9, 7463−7470

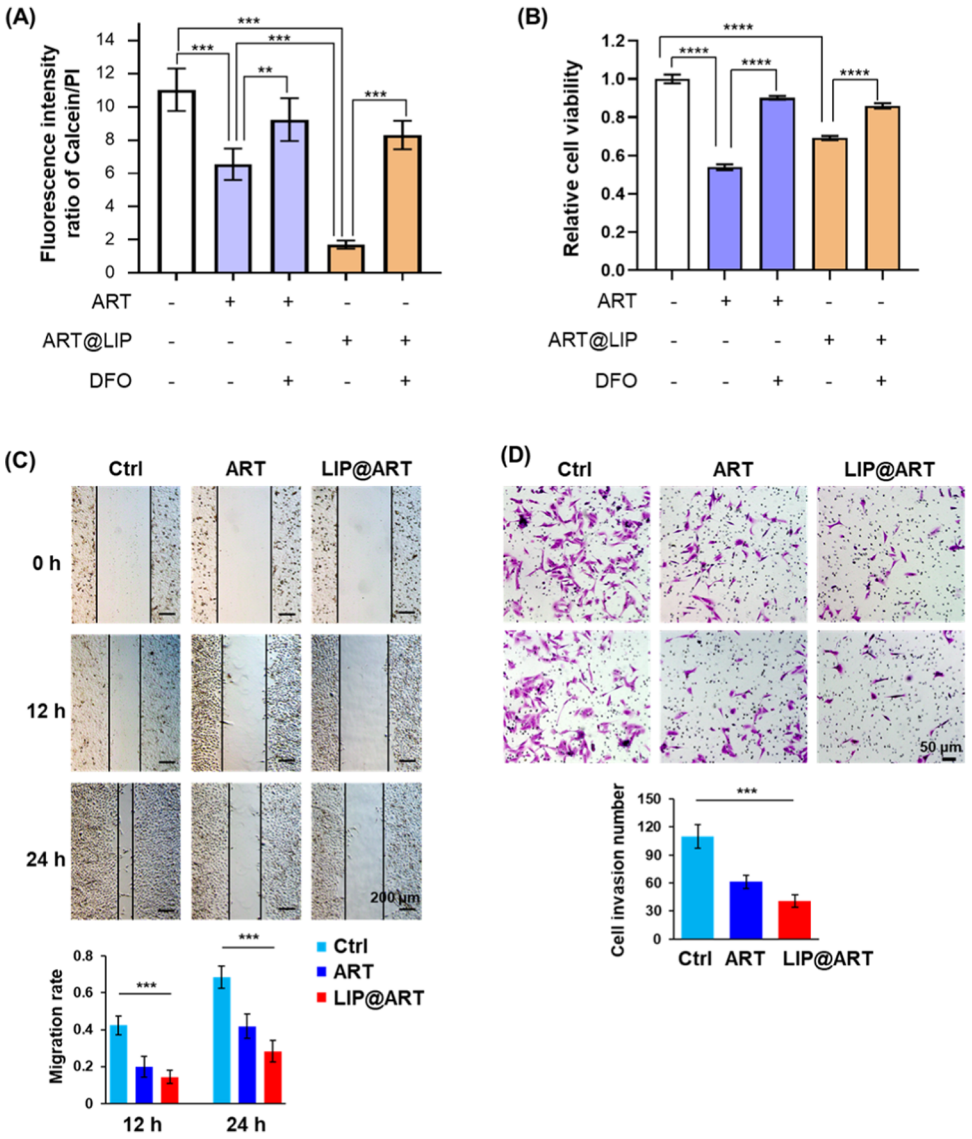

Figure 6. Preserved antitumor effect of LIP@ART in PTC cells. (A, B) Cell death of B-CPAP cells as measured by Calcein/PI cell viability assay (A) or Alamar Blue assay (B). After 24 h exposure to 200 μM ART or LIP@ART, the cells were stained by the Calcein/PI (n = 4) or Alamar Blue (n = 5) working solution (Beyotime, China) followed by fluorescence density measurement. $^{**}P < 0.01$, $^{***}P < 0.001$, and $^{****}P < 0.0001$. (C) Representative images and quantitation of B-CPAP cell migration in a wound healing assay (n = 5). Scale bar: 200 μm. (D) Representative images and quantitation of B-CPAP cell transwell invasion (n = 7). Scale bar: 50 μm. Data are presented as mean ± SD $^{***}P < 0.001$.

cells by upregulating the expression of heme oxygenase-1 (HO-1).[17] Neferine also induces ferroptosis in thyroid cancer cells by inhibiting Nrf2/HO-1/NQO1 signaling.[18] Vitamin C induces ferroptosis in anaplastic thyroid cancer (ATC), a rare but highly lethal thyroid cancer, by activating ferritinophagy.[19]

In summary, these results revealed the capacity of ART to induce ferroptosis in PTC cells via disordered iron homeostasis.

Synthesis and Characterization of Liposome-Encapsulated Artesunate, LIP@ART. The therapeutic effect of ART is limited by its low solubility, poor bioavailability, short half-life, and side effects.[11] Liposome is a safe and FDA-approved drug delivery system frequently used in the therapy of a variety of diseases, such as malaria and cancers.

To prepare LIP@ART, a thin-film rehydration method was employed using DSPC, cholesterol, DSP-PEG, and ART. TEM imaging showed that both liposome (LIP) and liposome-encapsulated ART (LIP@ART) had a sphere-like morphology (Figure 4A). The hydrodynamic sizes of LIP@ART (119.73 ± 5.86 nm) were slightly larger than those of LIP (113.86 ± 11.7 nm; Figure. 4B). Both LIP and LIP@ART showed negative surface charges, in which the ζ-potentials of LIP@ART (−25.76 ± 2.38 mV) were lower than those of LIP (−22.69 ± 2.09 mV; Figure 4B). UV−vis analysis revealed that the ART absorbance peak (204 nm) was observed in the absorbance spectra of ART and LIP@ART but not in LIP (Figure 4C), indicating the encapsulation of ART in LIP@ART. We constructed a standard curve using gradient-dosed ART to calculate the encapsulation efficiency (EE) (65.5%) and DLC (9.67%) of LIP (Figure 4D), demonstrating successful encapsulation and loading.

Preserved Ferroptotic and Antitumor Effect of LIP@ART in PTC Cells. After obtaining liposome-encapsulated ART, we measured the ferroptotic and antitumor effect of LIP@ART versus ART by evaluating ferroptosis induction, cell

https://doi.org/10.1021/acsomega.3c05226
ACS Omega 2024, 9, 7463−7470

invasion, and migration in B-CPAP cells. LIP@ART did not change the lipid peroxidation and percentage of ferroptotic B-CPAP cells compared to ART (Figure 5A), indicating that liposome encapsulation did not limit ART-driven ferroptosis induction. Mechanically, the protein content of GPX4 and SLC7A11 was decreased in ART- and ART@LIP-treated cells compared to untreated cells (Figure 5B). GPX4 plays a key role in protecting cells against excessive accumulation of lipid peroxides and ferroptosis, whereas SLC7A11 is a cystine/glutamate antiporter that regulates the intracellular levels of glutathione (GSH), an essential antioxidant for GPX4 function.[6,7] The level of 4-HNE, one of the primary products of lipid peroxidation,[6] was also increased by ART@LIP (Figure 5C). The iron chelator, DFO, recovered GPX4 and SLC7A11 protein contents and 4-HNE levels to some extent (Figure 5B,C). These results confirmed ferroptosis induction by ART and ART@LIP. However, an overall decrease in ACSL4 protein level was accompanied by treatment with ART and ART@LIP (Figure 5B). ACSL4 is an enzyme involved in the metabolism of polyunsaturated fatty acids (PUFAs). Upregulation of ACSL4 expression leads to increased incorporation of PUFAs into phospholipids of cell membranes, rendering cells more susceptible to lipid peroxidation.[6,7] This may exclude the involvement of ACSL4 in ART- and ART@LIP-induced ferroptosis.

We then evaluated the antitumor effects of ART and LIP@ART in PTC cells. As shown in Figure 6A,B, ART and ART@LIP significantly induced cell deaths ($P < 0.001$). Co-treatment with DFO substantially rescued cells from ART- ($P < 0.01$) and ART@LIP-induced cell death ($P < 0.001$; Figure 6A,B). Compared to the untreated cells, migration and invasion were significantly inhibited by ART and LIP@ART ($P < 0.001$; Figure 6C,D).

Liposome-based therapeutic strategies have been used in chemotherapy and gene therapy for breast,[20] colorectal,[21] and pancreatic cancers.[22] This study demonstrated that liposome encapsulation is a feasible strategy to deliver and preserve the antitumor effect of ART in PTC cells.

CONCLUSIONS

Ferroptosis resistance occurs in thyroid cancers, and ART induces ferroptosis in PTC cells. The liposome encapsulation of ART preserves efficiency in inducing ferroptosis of PTC cells and the antitumor effect by inhibiting the invasion and migration of PTC cells.

ASSOCIATED CONTENT

Supporting Information

The Supporting Information is available free of charge at https://pubs.acs.org/doi/10.1021/acsomega.3c05226.

Marker genes of ferroptosis curated from FerrDb (Table S1) (PDF)

AUTHOR INFORMATION

Corresponding Authors

Shuping Zhang − *The First Affiliated Hospital of Shandong First Medical University, Jinan, Shandong 250014, China; Medical Science and Technology Innovation Center, , Shandong First Medical University, Jinan, Shandong 250117, China;* orcid.org/0000-0003-1586-0559; Email: spzhang@sdfmu.edu.cn

Ling Gao − *Department of Endocrinology, Shandong Provincial Hospital, Shandong University, Jinan, Shandong 250021, China; Shandong Key Laboratory of Endocrinology and Lipid Metabolism, Jinan, Shandong 250021, China;* Email: linggao@sdu.edu.cn

Authors

Li Sun − *Department of Endocrinology, Shandong Provincial Hospital, Shandong University, Jinan, Shandong 250021, China; Shandong Key Laboratory of Endocrinology and Lipid Metabolism, Jinan, Shandong 250021, China; The First Affiliated Hospital of Shandong First Medical University, Jinan, Shandong 250014, China*

Guangzhe Zheng − *Medical Science and Technology Innovation Center, , Shandong First Medical University, Jinan, Shandong 250117, China*

Meng Zhou − *Department of Endocrinology, Shandong Provincial Hospital, Shandong University, Jinan, Shandong 250021, China; Shandong Key Laboratory of Endocrinology and Lipid Metabolism, Jinan, Shandong 250021, China*

Yingyu Zhang − *Medical Science and Technology Innovation Center, , Shandong First Medical University, Jinan, Shandong 250117, China*

Yashuang Yang − *Department of Endocrinology, Shandong Provincial Hospital, Shandong University, Jinan, Shandong 250021, China; Shandong Key Laboratory of Endocrinology and Lipid Metabolism, Jinan, Shandong 250021, China*

Complete contact information is available at: https://pubs.acs.org/10.1021/acsomega.3c05226

Author Contributions

L.S. and G.Z. performed the experiments. M.Z., Y.Z., and Y.Y. contributed to the experiments. S.Z. and L.G. designed the experiments and wrote the manuscript.

Funding

This work was supported under grants from the Natural Science Foundation of Shandong (grant numbers: ZR2022QB047) and the "Taishan Scholars" Program for Young Expert of Shandong Province (grant number: tsqn202103105).

Notes

The authors declare no competing financial interest.

REFERENCES

(1) Chen, D. W.; Lang, B. H. H.; McLeod, D. S. A.; Newbold, K.; Haymart, M. R. Thyroid cancer. *Lancet* **2023**, *401* (10387), 1531−1544.

(2) Siegel, R. L.; Miller, K. D.; Wagle, N. S.; Jemal, A. Cancer statistics, 2023. *Ca-Cancer J. Clin.* **2023**, *73* (1), 17−48.

(3) Agrawal, N.; Akbani, R.; Aksoy, B. A.; et al. Integrated genomic characterization of papillary thyroid carcinoma. *Cell* **2014**, *159* (3), 676−690, DOI: 10.1016/j.cell.2014.09.050.

(4) Ito, Y.; Miyauchi, A.; Kihara, M.; Fukushima, M.; Higashiyama, T.; Miya, A. Overall Survival of Papillary Thyroid Carcinoma Patients: A Single-Institution Long-Term Follow-Up of 5897 Patients. *World J. Surg.* **2018**, *42* (3), 615−622.

(5) Dixon, S. J.; Lemberg, K. M.; Lamprecht, M. R.; Skouta, R.; Zaitsev, E. M.; Gleason, C. E.; Patel, D. N.; Bauer, A. J.; Cantley, A. M.; Yang, W. S.; et al. Ferroptosis: an iron-dependent form of nonapoptotic cell death. *Cell* **2012**, *149* (5), 1060−1072.

(6) Zhang, S.; Xin, W.; Anderson, G. J.; Li, R.; Gao, L.; Chen, S.; Zhao, J.; Liu, S. Double-edge sword roles of iron in driving energy production versus instigating ferroptosis. *Cell Death Dis.* **2022**, *13* (1), No. 40, DOI: 10.1038/s41419-021-04490-1.

(7) Zhang, C.; Liu, X.; Jin, S.; Chen, Y.; Guo, R. Ferroptosis in cancer therapy: a novel approach to reversing drug resistance. *Mol. Cancer* **2022**, *21* (1), No. 47, DOI: 10.1186/s12943-022-01530-y.
(8) Daily, J. P.; Minuti, A.; Khan, N. Diagnosis, Treatment, and Prevention of Malaria in the US: A Review. *JAMA* **2022**, *328* (5), 460−471.
(9) Roh, J.-L.; Kim, E. H.; Jang, H.; Shin, D. Nrf2 inhibition reverses the resistance of cisplatin-resistant head and neck cancer cells to artesunate-induced ferroptosis. *Redox Biol.* **2017**, *11*, 254−262. Chen, Y.; Wang, F.; Wu, P.; Gong, S.; Gao, J.; Tao, H.; Shen, Q.; Wang, S.; Zhou, Z.; Jia, Y. Artesunate induces apoptosis, autophagy and ferroptosis in diffuse large B cell lymphoma cells by impairing STAT3 signaling. *Cell. Signalling* **2021**, *88*, No. 110167, DOI: 10.1016/j.cellsig.2021.110167.
(10) Xu, Z.; Liu, X.; Zhuang, D. Artesunate inhibits proliferation, migration, and invasion of thyroid cancer cells by regulating the PI3K/AKT/FKHR pathway. *Biochem Cell Biol.* **2022**, *100* (1), 85−92.
(11) Ruwizhi, N.; Maseko, R. B.; Aderibigbe, B. A. Recent Advances in the Therapeutic Efficacy of Artesunate. *Pharmaceutics* **2022**, *14* (3), No. 504, DOI: 10.3390/pharmaceutics14030504.
(12) Zhou, N.; Yuan, X.; Du, Q.; Zhang, Z.; Shi, X.; Bao, J.; Ning, Y.; Peng, L. FerrDb V2: update of the manually curated database of ferroptosis regulators and ferroptosis-disease associations. *Nucleic Acids Res.* **2023**, *51* (D1), D571−D582.
(13) Liu, W.; Chakraborty, B.; Safi, R.; Kazmin, D.; Chang, C.-y.; McDonnell, D. P. Dysregulated cholesterol homeostasis results in resistance to ferroptosis increasing tumorigenicity and metastasis in cancer. *Nat. Commun.* **2021**, *12* (1), No. 5103.
(14) Lin, R.; Fogarty, C. E.; Ma, B.; Li, H.; Ni, G.; Liu, X.; Yuan, J.; Wang, T. Identification of ferroptosis genes in immune infiltration and prognosis in thyroid papillary carcinoma using network analysis. *BMC Genomics* **2021**, *22* (1), No. 576, DOI: 10.1186/s12864-021-07895-6. Ren, X.; Du, H.; Cheng, W.; Wang, Y.; Xu, Y.; Yan, S.; Gao, Y. Construction of a ferroptosis-related eight gene signature for predicting the prognosis and immune infiltration of thyroid cancer. *Front. Endocrinol.* **2022**, *13*, No. 997873, DOI: 10.3389/fendo.2022.997873. Shi, J.; Wu, P.; Sheng, L.; Sun, W.; Zhang, H. Ferroptosis-related gene signature predicts the prognosis of papillary thyroid carcinoma. *Cancer Cell Int.* **2021**, *21* (1), No. 669, DOI: 10.1186/s12935-021-02389-7.
(15) Wang, Y.; Zheng, L.; Shang, W.; Yang, Z.; Li, T.; Liu, F.; Shao, W.; Lv, L.; Chai, L.; Qu, L.; et al. Wnt/beta-catenin signaling confers ferroptosis resistance by targeting GPX4 in gastric cancer. *Cell Death Differ.* **2022**, *29* (11), 2190−2202.
(16) Liu, M. Y.; Li, H. M.; Wang, X. Y.; Xia, R.; Li, X.; Ma, Y. J.; Wang, M.; Zhang, H. S. TIGAR drives colorectal cancer ferroptosis resistance through ROS/AMPK/SCD1 pathway. *Free Radical Biol. Med.* **2022**, *182*, 219−231.
(17) Chen, H.; Li, Z.; Xu, J.; Zhang, N.; Chen, J.; Wang, G.; Zhao, Y. Curcumin Induces Ferroptosis in Follicular Thyroid Cancer by Upregulating HO-1 Expression. *Oxid Med. Cell Longevity* **2023**, *2023*, No. 6896790.
(18) Li, S.; Zhang, Y.; Zhang, J.; Yu, B.; Wang, W.; Jia, B.; Chang, J.; Liu, J. Neferine Exerts Ferroptosis-Inducing Effect and Antitumor Effect on Thyroid Cancer through Nrf2/HO-1/NQO1 Inhibition. *J. Oncol.* **2022**, *2022*, No. 7933775.
(19) Wang, X.; Xu, S.; Zhang, L.; Cheng, X.; Yu, H.; Bao, J.; Lu, R. Vitamin C induces ferroptosis in anaplastic thyroid cancer cells by ferritinophagy activation. *Biochem. Biophys. Res. Commun.* **2021**, *551*, 46−53.
(20) Yang, B.; Song, B. P.; Shankar, S.; Guller, A.; Deng, W. Recent advances in liposome formulations for breast cancer therapeutics. *Cell. Mol. Life Sci.* **2021**, *78* (13), 5225−5243.
(21) Sang, R.; Stratton, B.; Engel, A.; Deng, W. Liposome technologies towards colorectal cancer therapeutics. *Acta Biomater.* **2021**, *127*, 24−40.
(22) Raza, F.; Evans, L.; Motallebi, M.; Zafar, H.; Pereira-Silva, M.; Saleem, K.; Peixoto, D.; Rahdar, A.; Sharifi, E.; Veiga, F.; et al. Liposome-based diagnostic and therapeutic applications for pancreatic cancer. *Acta Biomater.* **2023**, *157*, 1−23.

https://doi.org/10.1021/acsomega.3c05226
ACS Omega 2024, 9, 7463−7470